

PAPER • OPEN ACCESS

Cavity ringdown studies of the E–H transition in an inductively coupled oxygen plasma: comparison of spectroscopic measurements and modelling

To cite this article: Samuel D A Rogers *et al* 2022 *Plasma Sources Sci. Technol.* **31** 115006

View the [article online](#) for updates and enhancements.

You may also like

- [Black holes, gravitational waves and fundamental physics: a roadmap](#)
Abbas Askar, Chris Belczynski, Gianfranco Bertone *et al.*
- [Optical trapping and laser-spectroscopy measurements of single particles in air: a review](#)
Chuji Wang, Yong-Le Pan and Gorden Videen
- [Fiber loop ringdown gas flow sensors](#)
Haifa Alali and Chuji Wang



Analysis Solutions for your **Plasma Research**

- Knowledge,
- Experience,
- Expertise

[Click to view our product catalogue](#)

Contact Hiden Analytical for further details:
 www.HidenAnalytical.com
 info@hiden.co.uk



Surface Science

- ▶ Surface Analysis
- ▶ SIMS



3D depth Profiling

- ▶ Nanometre depth resolution



Plasma Diagnostics

- ▶ Plasma characterisation
- ▶ Customised systems to suit plasma Configuration



Mass and energy analysis of plasma ions

- ▶ Characterisation of neutrals and radicals

Cavity ringdown studies of the E–H transition in an inductively coupled oxygen plasma: comparison of spectroscopic measurements and modelling

Samuel D A Rogers¹, Amelia Bond¹, Benjamin J Rhodes², Robert Peverall, Gus Hancock and Grant A D Ritchie*

Department of Chemistry, Physical and Theoretical Chemistry Laboratory, The University of Oxford, South Parks Road, Oxford OX1 3QZ, United Kingdom

E-mail: grant.ritchie@chem.ox.ac.uk

Received 29 June 2022, revised 18 October 2022

Accepted for publication 25 October 2022

Published 9 November 2022



Abstract

The absolute number density of ground state oxygen atoms, $O(^3P)$, present in a 100 mTorr oxygen plasma has been determined as a function of operating power using cavity ringdown spectroscopy (CRDS). The dissociation fraction increases by an order of magnitude from $\sim 0.8\%$ at 50 W to 8% at 250 W and reflects a similar increase in the electron density over this power range. Emission spectra show that the E–H switchover is accompanied by increased rotational heating of O_2 and this behaviour is also observed in the translational temperatures determined by fitting the Doppler limited $O(^3P)$ CRDS data. The measurements are contextualised via a volume averaged kinetic model that uses the measured absolute densities of $O(^3P)$ and $O_2(a^1\Delta_g, v=0)$ as a function of power as its benchmarks. Despite the inherent spatial inhomogeneity of the plasma, the volume averaged model, which uses a minimal set of reactions, is able to both reproduce previous measurements on the absolute density of O^- and to infer physically reasonable values for both the electron temperature and number density as the E–H switch over is traversed. Time-resolved emission measurements return a value of 0.2 for the wall loss coefficient for $O_2(b^1\Sigma_g^+)$; as a consequence, the number density of $O_2(b^1\Sigma_g^+)$ is (at least) one order of magnitude less than $O_2(a^1\Delta_g)$.

Keywords: inductively coupled plasma, oxygen plasma, atomic oxygen, singlet oxygen, cavity ringdown spectroscopy, optical emission spectroscopy, mode transition

(Some figures may appear in colour only in the online journal)

* Author to whom any correspondence should be addressed.

¹Current address: British Antarctic Survey, High Cross, Madingley Road, Cambridge, CB3 0ET, United Kingdom.

²Current address: Yusuf Hamied Department of Chemistry, University of Cambridge, Cambridge, CB2 1EW, United Kingdom.



Original content from this work may be used under the terms of the [Creative Commons Attribution 4.0 licence](https://creativecommons.org/licenses/by/4.0/). Any further distribution of this work must maintain attribution to the author(s) and the title of the work, journal citation and DOI.

1. Introduction

Oxygen based inductively coupled plasmas (ICPs) are of both practical and fundamental interest, finding extensive applications in industry while also constituting an example of an electronegative plasma (a plasma in which negative ions play a significant role). There has been much work, both experimental and theoretical [1–8], aimed at understanding these complex systems including analysis of the switch from the capacitive E-mode observed at low power to the technologically important, higher electron density, inductive H-mode seen at higher powers [9].

The chemistry and physics of these plasmas is heavily influenced not only by the presence of negative ions, but also high densities of ground state atoms, $O(^3P)$, and electronically excited molecules, particularly the low-lying metastable $O_2(a^1\Delta_g)$ state. These species are therefore highly desirable targets for detection as well as important indicators of the behaviour of the plasma as a whole. Indeed, such is their importance that comparisons between experimental measurements of these species and densities predicted by kinetic modelling is a cornerstone of efforts to better understand the plasma behaviour [10, 11]. Reliable measurements of these key species are of the utmost importance. Extensive accounts of the numerous techniques employed to measure them are available elsewhere [10, 12] and here we give a brief overview.

One quantitative detection technique is laser absorption spectroscopy, but in the cases of $O(^3P)$ and $O_2(a^1\Delta_g)$ a lack of electric-dipole allowed transitions coincident with the wavelengths at which lasers are readily available makes this difficult. For this reason much of the work to detect these species has used alternative methods. For $O(^3P)$ the main detection techniques are two-photon laser induced fluorescence (TALIF) [13, 14] and optical emission based actinometry [15, 16]. TALIF requires knowledge of the two-photon excitation cross sections for $O(^3P)$ and for a calibrant gas (usually xenon) [17, 18] while actinometry requires both the addition of a perturbing chemical actinometer to the system and meticulous calibration in order to achieve absolute densities. Even fewer techniques exist to quantify the first excited state of O_2 . Once again actinometry measurements (on the forbidden $O_2(a^1\Delta_g) \rightarrow O_2(X^3\Sigma_g^-)$ band) have been used [10], but such emission is very weak and requires precise knowledge of the emitting volume of the plasma and the solid angle which the detector occupies in order to interpret results quantitatively.

Despite the lack of readily accessible allowed transitions, absorption based detection is not out of the question for either species. Indeed both have been detected using VUV spectroscopy, typically around 130 nm [2, 19]. The lack of lasers at these wavelengths means that alternative radiation sources are required and both synchrotron radiation [19] and UV lamps [20] have been used. These sources have relatively broad linewidths and as a result the source lineshape must be carefully accounted for when analysing spectra. Additionally any self absorption within the source must be accounted for [20]. A further complicating factor is that $O(^3P)$ and $O_2(a^1\Delta_g)$

absorb very strongly in the VUV and so detection may take place under optically thick conditions.

Recently a method was demonstrated of inferring concentrations of both $O(^3P)$ and $O_2(a^1\Delta_g)$ from the recovery dynamics of the O_2 ground state (measured using the Schumann–Runge (S–R) continuum absorption) after a DC glow discharge was extinguished [10]. This technique also allowed the extraction of lifetimes for both species, but it is an indirect measurement and relies on the assumption that $O(^3P)$ and $O_2(a^1\Delta_g)$ are the only species that produce $O_2(X^3\Sigma_g^-)$ when the plasma is extinguished. It also requires that both species are lost at significantly different rates. Additionally, the use of the S–R continuum requires VUV radiation and the temperature dependence of the continuum absorption cross-section adds significant uncertainty to measurements unless they are limited to the late afterglow where temperatures are ambient.

Absorption measurements are also possible without the use of VUV radiation. The forbidden transitions between the low lying states of atomic and molecular oxygen can be probed, but because of their electric quadrupole ($O_2(a^1\Delta_g)$) or magnetic dipole ($O(^3P)$) nature they require enhanced absorption techniques to be measurable. Given the difficulties in performing other methods of detection and the convenience of radiation sources in the visible and near-IR regions, i.e. those required to probe the aforementioned forbidden transitions, it is therefore unsurprising that a range of cavity enhanced methods has been used to detect these two species. $O(^3P)$ has been detected (using the $O(^1D_2) \leftarrow O(^3P_{2,1})$ transitions around 630 nm) by intra-cavity laser absorption spectroscopy (ICLAS) in a flow tube [21], by pulsed cavity ringdown spectroscopy (CRDS) in a microwave discharge [22], and by off-axis integrated cavity output spectroscopy (ICOS) in an ICP at 10–40 Torr [23]. Measurements have also been made in an ICP operating at pressures of 10–100 mTorr, first using cavity enhanced absorption spectroscopy [24] and most recently using a continuous wave (cw) CRDS arrangement [12].

$O_2(a^1\Delta_g)$ measurements have utilised the Noxon system ($O_2(b^1\Sigma_g^+) \leftarrow O_2(a^1\Delta_g)$) on the (0, 0) and (1, 0) bands at ca. 1900 nm and 1500 nm respectively. The first absorption measurements of this species were made by ICLAS in a flow tube (1–5 Torr) on the (0, 0) band [25]. Later measurements, utilizing off-axis ICOS, were the first to observe the (1, 0) band, this time in the afterglow of a 20–32 Torr ICP [26, 27] and later in the afterglow of a 28 Torr microwave discharge [28]. Földes *et al* demonstrated detection on the (1, 0) band using cw-CRDS in a 2.25 Torr microwave plasma [29] and most recently $O_2(a^1\Delta_g)$ was probed using cw-CRDS on the (0, 0) band in an ICP at 100 mTorr [30].

In this paper we expand on our previous measurements by investigating the variation in $O(^3P)$ density, $[O(^3P)]$, as the plasma transitions between capacitive and inductive modes using cw-CRDS, with these results augmented by emission spectra taken on the oxygen A-band ($O_2(b^1\Sigma_g^+) \rightarrow O_2(X^3\Sigma_g^-)$). These results are presented in section 3 and are contextualised by combining them with previous measurements of the absolute number densities of $O_2(a^1\Delta_g)$ in its ground vibrational level, $[O_2(a, v = 0)]$ [30], in order to

inform a volume averaged kinetic plasma model. This model is outlined in section 4 and although it employs only a relatively small number of reactions. We show in section 5 that it is capable of returning predictions of the most abundant atomic and molecular ions and neutrals, as well as the electron density, $[e^-]$. The physico-chemical parameters of the plasma, as determined both by experiment and modelling, are then discussed in section 6 with conclusions presented in section 7. In the next section we outline our experimental method.

2. Experimental details

The experimental work was carried out using a water-cooled cylindrical plasma chamber described previously [12]. The water-cooled chamber is predominantly constructed of aluminium and measures 21 cm \times 35 cm (height \times diameter). The chamber pressure is maintained at 100 mTorr for all measurements. The chamber is fitted with a pair of vacuum mirror mounts separated from the main chamber by narrow diameter (id \sim 9 mm) baffle arms to protect the mirrors from the plasma environment. Pure O_2 (99.999% BOC) is delivered into the chamber via these arms at a constant flow of 10 sccm. Power (0–300 W; 13.56 MHz) is supplied to the chamber by a 1.5 turn, planar, double-spiral antenna with a diameter of \sim 20 cm and separated from the plasma by a fused silica window. Impedance matching is achieved by a homemade tuneable matching network.

In order to optically probe the plasma two high reflectivity mirrors ($R > 99.995\%$ Layertec GmbH, Germany) are housed in the vacuum mirror mounts forming an optical cavity and enabling CRDS to be performed as detailed previously [12, 30]. A general CRDS experimental arrangement [31] is depicted in figure 1. In such an experiment a cw laser excites a resonant mode of the cavity, and when the intensity of radiation in this mode reaches a predefined threshold value, the acousto-optic modulator (AOM) is triggered and acts as a fast switch to stop the laser beam entering the cavity thus beginning a ringdown event. The characteristic exponential decay time of the radiation intensity reflects the losses in the cavity both from the mirrors and from absorption. By stepping the laser over the absorption feature and averaging several hundred (typically 250 in this work) ringdown events at each wavelength, a spectrum can be produced. Measurements of $O(^3P)$ were carried out using an external cavity diode laser (ECDL, Toptica GmbH, Germany) which utilises a Littrow feedback arrangement and operates in the range 629–635 nm. Ringdown signals were detected using a photomultiplier tube (PMT). The optical emission from the plasma was monitored by a silicon photodiode and the PMT whilst wavelength-resolved emission spectra were obtained by imaging the plasma, via a large core multimode optical fibre, into a spectrograph (Andor Shamrock 303i). Optical emission measurements provide a quick and convenient way to monitor the plasma and provides information complementary to that provided by CRDS. Measurements are made of $[O(^3P)]$ as a function of power, stepping in intervals of 50 W across most of the power range, with smaller steps of 20 W used to investigate the E–H switchover region.

3. Experimental results and analysis

3.1. Emission measurements

The upper panel of figure 2(a) shows a sample of raw emission data taken on the oxygen A-band ($O_2(b^1\Sigma_g^+) \rightarrow O_2(X^3\Sigma_g^-)$) gathered at 100 mTorr pressure and operating powers between 50 and 300 W. The dominant feature in all the spectra is the (0, 0) vibrational band. The increase in emission intensity (which is also visible to the naked eye) between 120 W and 140 W provides strong evidence of the E–H switchover. Previous observations in this chamber support this interpretation [30]. Both the broadband optical emission from the plasma and atomic emission at 777 nm also show a marked increase in intensity above 120 W.

Although emission spectra are limited in their ability to provide absolute number densities it is expected that the integrated area under the emission band is proportional to the $O_2(b^1\Sigma_g^+)$ density, $[O_2(b)]$. The results of numerical integration of the emission spectra are shown in the inset to figure 2(a). It is notable that from 140 W up to 300 W the total emission changes little, indicating an approximately constant $[O_2(b)]$. However, over this power range, emission from higher rotational states increases in intensity whilst that from lower rotational states becomes less intense, and is evidence of rotational heating. Likewise the increasing emission on the (1, 1) band (above 768 nm) is also evidence of internal heating, in this case, in the vibrational mode. Extraction of a reliable temperatures from these spectra can be achieved via a contour fit with a PGOPHER [32] simulation (with molecular constants and Franck–Condon factors from Yu *et al* [33] and the magnetic dipole moment from Drouin *et al* [34]). The lower panel of figure 2(a) shows an example fit to the emission spectrum taken at 300 W and returns a rotational temperature $T_{rot} = 629 \pm 10$ K and a vibrational temperature of $T_{vib} = 905 \pm 40$ K (errors are estimated by repeatedly fitting the spectrum with different initial parameters to establish the reproducibility of the optimised fit). Fits to spectra at other powers produced the rotational temperatures displayed in figure 2(b) and show a smooth trend of increasing T_{rot} with increasing power from \sim 350 K in the CCP regime up to \sim 630 K in the ICP regime. The E–H mode transition is clearly present, as a sharp rise in temperature, again between 120 and 140 W. The low intensity of the (1, 1) emission for power below 300 W precluded the accurate determination of T_{vib} under these conditions.

It should be noted that these emission derived temperatures should be treated with caution because the data is necessarily weighted towards the hottest (and brightest) regions of the plasma, meaning that the temperatures derived are not representative of the bulk but instead indicate a lower bound on the maximum temperature within the plasma [3]. Additional uncertainty is introduced by the need to correct the raw data for the wavelength dependence of the spectrograph and the CCD quantum efficiencies. Nevertheless, the data do provide a good qualitative guide to trends in internal excitation within the plasma.

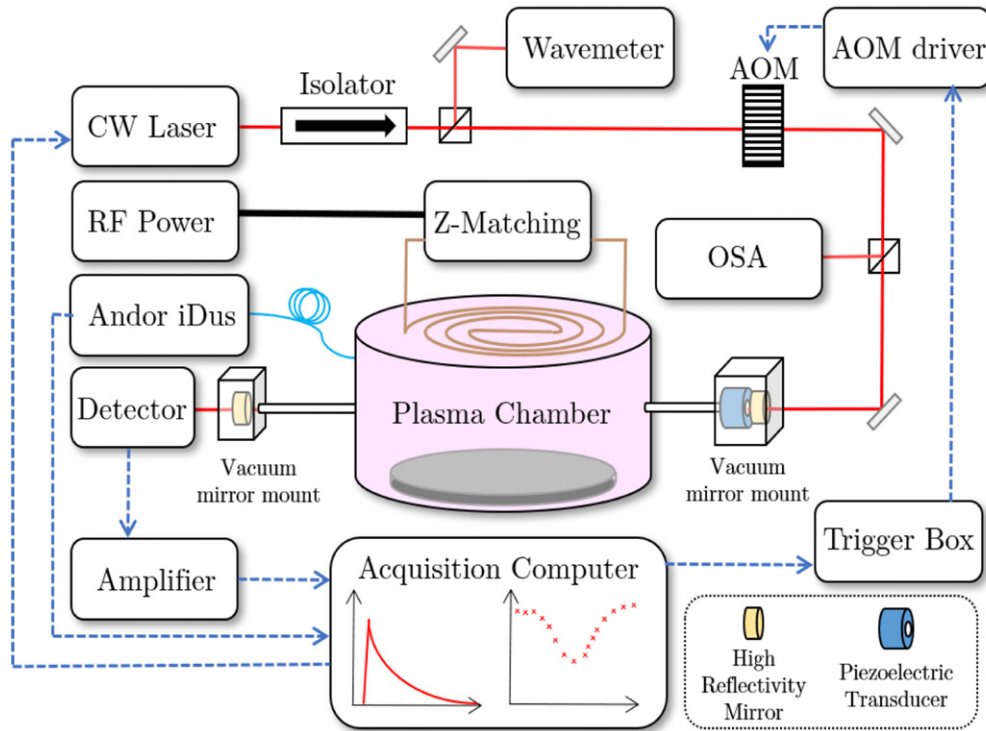


Figure 1. A schematic of our experimental arrangement. For cavity ringdown measurements cw laser radiation passes through an isolator and an AOM and is then coupled into the optical cavity. Detection and amplification allow ringdown signals to be recorded and spectra produced. The laser wavelength and stability are monitored by use of a wavemeter and an optical spectrum analyser respectively. Optical emission spectra are recorded using an Andor Shamrock spectrograph with iDus CCD camera.

Loss of species at plasma chamber walls is one of the biggest sources of uncertainty in plasma modelling and makes direct measurement of wall loss rates very desirable. These rates have been measured previously for $O(^3P)$ [12] and $O_2(a^1\Delta_g)$ [30] and we now present a measurement of wall loss for $O_2(b^1\Sigma_g^+)$ in our chamber obtained by time resolved observation of the $b \rightarrow X$ emission. A 760 nm optical filter (FWHM = 10 nm) was placed in front of a PMT, chosen for its high sensitivity and fast response time (~ 1 ns), to restrict the emission incident on the detector to that arising from the A-band. The plasma was then modulated on and off (between 0 and 200 W) and the decay in emission from the b state measured. Although multiple processes contribute to the destruction of $O_2(b^1\Sigma_g^+)$ (see later), loss at the chamber walls is the only important loss process that persists for more than a few ms after the plasma is extinguished. Lifetimes of 6.7 ± 0.5 ms and 2.4 ± 0.3 ms were determined at 100 mTorr and 10 mTorr respectively, from single exponential fits to the time-resolved data. These lifetimes are significantly shorter than those measured for $O(^3P)$ [12] and $O_2(a^1\Delta_g)$ [30] (~ 100 ms), indicating that $O_2(b^1\Sigma_g^+)$ wall loss lies much closer to the diffusion dominated regime.

3.2. Cavity ringdown spectroscopy (CRDS) measurements

Here we expand on our previous work measuring $O(^3P)$ using CRDS and investigate the variation in $[O(^3P)]$ with plasma power. We use the electric dipole forbidden $O(^1D_2) \leftarrow O(^3P_2)$

transition. CRD spectra can be produced from measured ringdown times according to:

$$\alpha(v) = \frac{1}{c} \left(\frac{1}{\tau(v)} - \frac{1}{\tau_0(v)} \right), \quad (1)$$

where $\alpha(v)$ is the absorption coefficient, c is the speed of light, $\tau_0(v)$ is the ringdown time without absorber (determined by fitting a baseline to the CRD spectra) and $\tau(v)$ is the ringdown time with absorber present. Exemplar spectra are shown in figure 3(a) along with Gaussian fits to the data. Doppler broadening dominates at low pressure allowing direct calculation of translational temperatures, T_{trans} (red points in figure 3(b)). The full width at half maximum (FWHM), Δv , of a Doppler broadened spectral line is related to T_{trans} by:

$$\frac{\Delta v}{v} = \sqrt{\frac{8k_B T_{\text{trans}} \ln 2}{mc^2}}, \quad (2)$$

where v is the absolute frequency of the transition and m is the mass of the absorbing species.

Gaussian lineshape fitting also allows the determination of integrated absorption coefficients, α_{INT} , from which line-of-sight averaged densities, N_{avg} , are then extracted using, $\alpha_{\text{INT}} = \sigma_{\text{INT}} N_{\text{avg}}$ where the integrated cross section for the transition, σ_{INT} , is calculated from the Einstein A-factor according to:

$$\sigma_{\text{INT}} = \frac{g_2 A_{21} c^2}{g_1 8\pi v^2}, \quad (3)$$

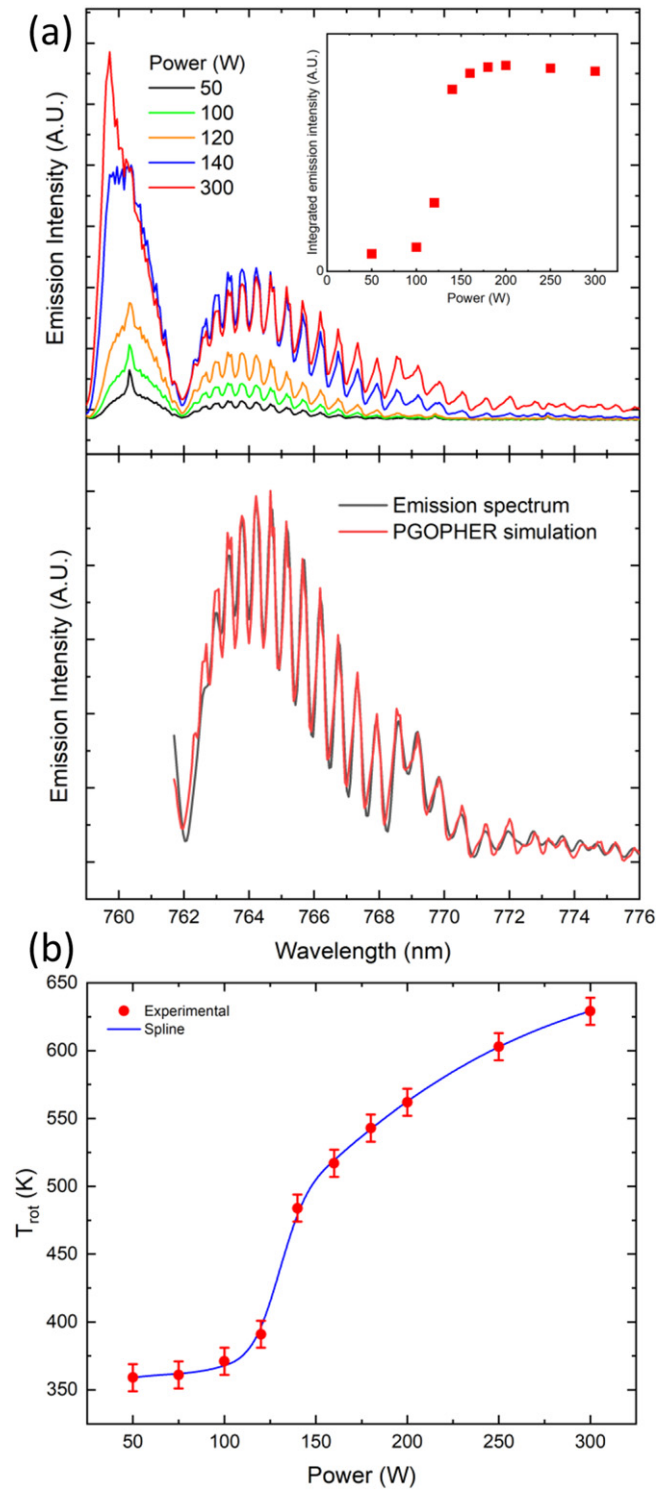


Figure 2. (a) (Upper panel) Emission on the oxygen A-band ($\text{O}_2(b) \rightarrow \text{O}_2(X)$) as a function of plasma power showing evidence of E–H mode switchover and rotational and vibrational heating. (Inset) Integrated area of the A-band emission as a function of power, indicating the trend in $[\text{O}_2(b)]$. (Lower panel) PGOPHER fit to the 300 W data (adjusted for spectrometer efficiency) yielding $T_{\text{rot}} = 629 \pm 10$ K and $T_{\text{vib}} = 905 \pm 40$ K. (b) Rotational temperature as a function of power as determined by contour fitting to emission data with a spline interpolation shown in blue.

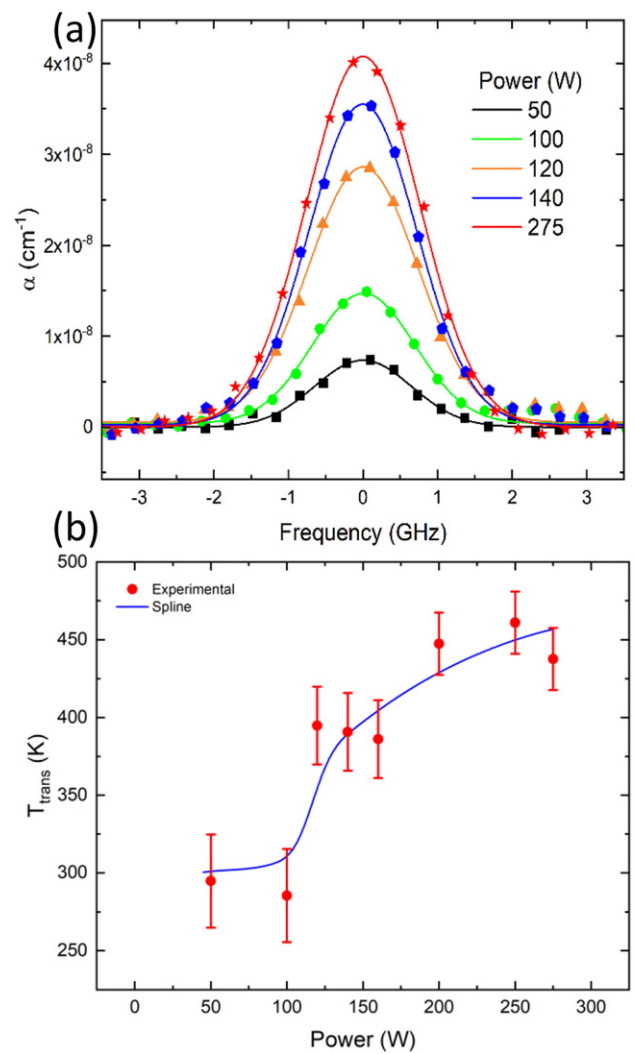


Figure 3. (a) Example CRD spectra of the $\text{O}(^1\text{D}_2) \leftarrow \text{O}(^3\text{P}_2)$ transition as a function of power. Each spectrum includes a Gaussian fit. (b) Translational temperatures of atomic oxygen as a function of plasma power determined from Doppler widths of fits to the spectra. Also included is a smoothed spline which is used to estimate temperatures used in volume averaged modelling (see later).

where $g_2 = g_1 = 5$. $A_{21} = 5.65 \times 10^{-3} \text{ s}^{-1}$ [35] yielding an integrated cross section of $2.98 \times 10^{-23} \text{ cm}^2 \text{ cm}^{-1}$. The average density in the plasma region (i.e. excluding the baffle arms which are predominantly filled with cold $\text{O}_2(X^3\Sigma_g^-)$ rather than plasma) is then calculated by adjusting the line-of-sight average value by a factor of 77/36 which accounts for the length of the baffle arms and for diffusion of atoms into the arms [12]. The total density in all three $\text{O}(^3\text{P})$ spin-orbit states is shown in figure 4 and is calculated from the measured $[\text{O}(^3\text{P}_2)]$ (also shown in figure 4) by using statistical mechanics and the T_{trans} values. The validity of this method, which predicts the populations of $\text{O}(^3\text{P}_1)$ and $\text{O}(^3\text{P}_0)$ from the measured population of $\text{O}(^3\text{P}_2)$ was confirmed previously [12] by CRDS measurements of $\text{O}(^3\text{P}_1)$. The total atom density, $[\text{O}(^3\text{P})]$ can

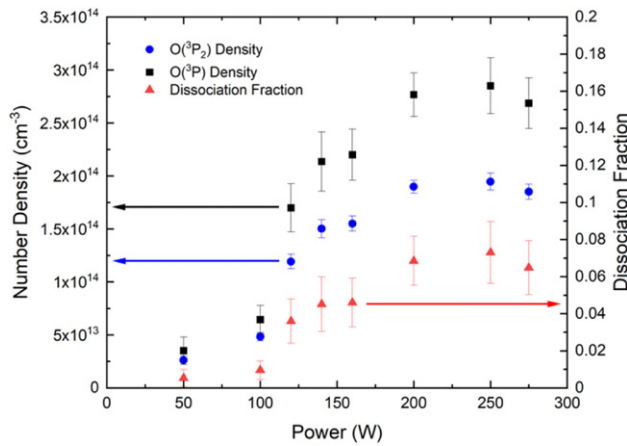


Figure 4. Line-of-sight average number densities of atomic oxygen in the lowest spin orbit state $O(^3P_2)$ (blue) and total $O(^3P)$ densities (black) derived from statistical thermodynamics. Also shown are dissociation fractions, calculated according to equation (4).

then be used to calculate the dissociation fraction, δ , in the plasma according to:

$$\delta = \frac{[O(^3P)]}{2[O_2]} \quad (4)$$

where $[O_2]$ is the density of O_2 molecules that would exist at the plasma temperature if all the atoms were to spontaneously recombine. Dissociation fractions are shown in figure 4.

The measured temperatures and δ values both show similar trends, with a rapid increase between 100 and 120 W and then a more gradual increase within the H-mode before eventually plateauing at the highest powers. T_{trans} values appear approximately ambient at ~ 300 K in the E-mode and show evidence of heating to ~ 450 K at the highest powers studied; δ in the E-mode is < 0.01 and increases by nearly an order of magnitude as the power is increased to 300 W. The E/H-mode switchover power measured by CRDS agrees well with that observed by emission. There is however a noticeable difference in the magnitudes of the temperatures measured by the two techniques, with the CRDS measurements consistently cooler. The difference in temperature is ca. 50 K in the E-mode, increasing to ~ 150 K in the H-mode. This discrepancy is likely a result that, while emission measurements are weighted towards the brightest and hottest regions of the plasma, CRDS is a line-of-sight average technique, and probes gas in cooler regions of the plasma. Another major difference is the significantly larger uncertainties on the CRDS derived values, the main source of which is the difficulty in fitting the baseline to the ringdown data, particularly at lower powers where the baseline variation is significant compared to the size of the absorption signal. The choice of baseline subtly alters the area and width of the absorption profile and results in a significant uncertainty in T_{trans} , which propagates through the statistical mechanics and affects δ .

4. Volume averaged kinetic model

A volume averaged kinetic model was constructed and used to interpret our measurements. Much prior work exists on the modelling of oxygen ICPs at a range of pressures [11, 36] and the reliability of such models relies heavily on the accuracy of rate coefficients available in the literature. Additionally, judging which reactions are most important and need to be included depends on the plasma conditions, e.g. termolecular reactions can be neglected at low pressure but can become important at high pressure. As the name suggests, inherent in a volume averaged model is the assumption that the plasma is spatially uniform throughout its volume (~ 20 l for our chamber). Although this assumption is never strictly true, and chemistry can vary spatially, particularly near the chamber walls, such models can still prove quantitatively and qualitatively useful. We aim here to select a reaction set capable of providing a reasonable quantitative agreement with experimental observations while retaining minimal complexity. We thus exclude excited molecular states above the b state, the second excited state of the atom $O(^1S)$ [37] and the ions O^+ [36] and O_2^- [11].

4.1. The reaction set

4.1.1. Electron impact rate coefficients. Rate coefficients, $k(T_e)$, for electron impact processes are given in table 1 and for computational convenience are expressed in Arrhenius form:

$$k(T_e) = aT_e^b \exp\left(\frac{-c}{T_e}\right), \quad (5)$$

where T_e is the electron temperature (in eV) and a , b and c are constants. Rate coefficients in this form were either deduced from the reported T_e dependence of literature values or determined by us from literature cross-sections, in order to find the values of a , b and c that provided the best fit for $T_e < 4$ eV (i.e. the electron temperatures likely to be present in our plasma). When only collision cross sections, $\sigma(E)$, are available we calculate the rate coefficients, k , and assume a Maxwellian electron energy distribution function (EEDF), $f(E)$, such that:

$$k(T_e) = \sqrt{\frac{2}{m_e}} \int_0^\infty E^{\frac{1}{2}} \sigma(E) f(E) dE, \quad (6)$$

where m_e is the mass of an electron. Equation (6) can then be well approximated by a rate coefficient in Arrhenius form. We also use the latest available rate coefficient and cross-section data, particularly those from Laporta *et al* [39] and Tashiro *et al* [41].

4.1.2. Heavy species rate coefficients. Rate coefficients for reactions between heavy species are given in table 2 in terms of their translational temperature, T_{trans} . Over the entire temperature range modelled, the rate coefficients of the processes in table 2 vary by no more than 18%; they are thus approximately constant for all our modelled conditions.

Table 1. Electron impact reactions and rate coefficients (T_e in eV).

#	Reaction	Rate coefficient/cm ³ s ⁻¹	Source
1	$e^- + O_2(X^3\Sigma_g^-) \rightarrow 2O(^3P) + e^-$	$1.74 \times 10^{-8} T_e^{-0.71} \exp(-7.19/T_e)$	[38] ^a
2	$e^- + O_2(a^1\Delta_g) \rightarrow 2O(^3P) + e^-$	$1.42 \times 10^{-8} T_e^{-0.65} \exp(-6.12/T_e)$	[38] ^a
3	$e^- + O_2(b^1\Sigma_g^+) \rightarrow 2O(^3P) + e^-$	$1.22 \times 10^{-8} T_e^{-0.6} \exp(-5.37/T_e)$	[38] ^a
4	$e^- + O_2(X^3\Sigma_g^-) \rightarrow O(^3P) + O(^1D) + e^-$	$1.08 \times 10^{-7} T_e^{-0.64} \exp(-9.45/T_e)$	[38] ^a
5	$e^- + O_2(a^1\Delta_g) \rightarrow O(^3P) + O(^1D) + e^-$	$8.26 \times 10^{-8} T_e^{-0.51} \exp(-8.27/T_e)$	[38] ^a
6	$e^- + O_2(b^1\Sigma_g^+) \rightarrow O(^3P) + O(^1D) + e^-$	$6.83 \times 10^{-8} T_e^{-0.42} \exp(-7.45/T_e)$	[38] ^a
7	$e^- + O_2(X^3\Sigma_g^-) \rightarrow O(^3P) + O^-$	$8.01 \times 10^{-10} T_e^{-1.17} \exp(-5.57/T_e)$	[39]
8	$e^- + O_2(a^1\Delta_g) \rightarrow O(^3P) + O^-$	$2.34 \times 10^{-9} T_e^{-1.13} \exp(-4.52/T_e)$	[39]
9	$e^- + O_2(b^1\Sigma_g^+) \rightarrow O(^3P) + O^-$	$1.98 \times 10^{-9} T_e^{-1.1} \exp(-3.88/T_e)$	[39]
10	$e^- + O_2(X^3\Sigma_g^-) \rightarrow O_2^+ + 2e^-$	$2.34 \times 10^{-9} T_e^{1.03} \exp(-12.29/T_e)$	[40]
11	$e^- + O_2(a^1\Delta_g) \rightarrow O_2^+ + 2e^-$	$2.34 \times 10^{-9} T_e^{1.03} \exp(-11.31/T_e)$	[40] ^b
12	$e^- + O_2(b^1\Sigma_g^+) \rightarrow O_2^+ + 2e^-$	$2.34 \times 10^{-9} T_e^{1.03} \exp(-10.66/T_e)$	[40] ^b
13	$e^- + O_2(X^3\Sigma_g^-) \rightarrow O_2(a^1\Delta_g) + e^-$	$1.02 \times 10^{-9} T_e^{0.12} \exp(-2.03/T_e)$	[41]
14	$e^- + O_2(a^1\Delta_g) \rightarrow O_2(X^3\Sigma_g^-) + e^-$	$1.53 \times 10^{-9} T_e^{0.12} \exp(-1.05/T_e)$	[41] ^c
15	$e^- + O_2(X^3\Sigma_g^-) \rightarrow O_2(b^1\Sigma_g^+) + e^-$	$4.23 \times 10^{-10} T_e^{-0.04} \exp(-2.78/T_e)$	[41]
16	$e^- + O_2(b^1\Sigma_g^+) \rightarrow O_2(X^3\Sigma_g^-) + e^-$	$1.27 \times 10^{-9} T_e^{-0.04} \exp(-1.153/T_e)$	[41] ^c
17	$e^- + O_2(a^1\Delta_g) \rightarrow O_2(b^1\Sigma_g^+) + e^-$	$2.75 \times 10^{-9} T_e^{-0.01} \exp(-0.82/T_e)$	[41]
18	$e^- + O_2(b^1\Sigma_g^+) \rightarrow O_2(a^1\Delta_g) + e^-$	$5.50 \times 10^{-9} T_e^{-0.01} \exp(-0.17/T_e)$	[41] ^c
19	$e^- + O(^3P) \rightarrow O(^1D) + e^-$	$4.54 \times 10^{-9} \exp(-2.36/T_e)$	[40]
20	$e^- + O(^1D) \rightarrow O(^3P) + e^-$	$8.17 \times 10^{-9} \exp(-0.4/T_e)$	[40]
21	$e^- + O^- \rightarrow O(^3P) + 2e^-$	$5.47 \times 10^{-8} T_e^{0.324} \exp(-2.98/T_e)$	[40]
22	$e^- + O_2^+ \rightarrow 2O(^3P, ^1D)$	$1.47 \times 10^{-8} T_e^{-0.9}$	[42] ^{a,d}

^aCalculated from a best fit in the form of equation (5) ($T_e < 4$ eV) as explained in the text.^bEstimated by adjusting the threshold of reaction 10.^cCalculated by detailed balancing using the rate coefficient of the corresponding excitation process, see for example Gudmundsson [40].^dProduces $O(^3P)$ and $O(^1D)$ in $\sim 1:1$ ratio via three channels ($2O(^3P)$, $2O(^1D)$ or $O(^3P) + O(^1D)$) [42].

We note that recent work [43, 44] has suggested that reactive quenching by $O(^3P)$ may be an important loss process for metastable oxygen molecules at high temperatures. However, for our highest atom density ($\sim 3 \times 10^{14}$ cm⁻³) and temperature (~ 450 K) the rate coefficients reported previously suggest lifetimes against this quenching process of ~ 6000 s for $O_2(a^1\Delta_g)$ and ~ 124 ms for $O_2(b^1\Sigma_g^+)$. The observed lifetimes for both these species are significantly shorter than these calculations suggest and so we conclude that $O(^3P)$ quenching is unimportant under the conditions in our chamber.

4.1.3. Wall loss coefficients. The rate of wall loss is influenced by surface material, chamber dimensions, temperature and diffusion coefficients. The relationship between these factors and the wall loss rate constant, k_L , was discussed at length by Chantry [45] and is given approximately by:

$$\frac{1}{k_L} = \tau = \frac{p\Lambda_0^2}{D} + \frac{2l_0(2-\gamma)}{v\gamma}, \quad (7)$$

where D is the diffusion coefficient for the species being lost at the wall. l_0 is the chamber's volume to surface area ratio (here

4.8 cm), v is the mean speed of the diffusing species and Λ_0 is given by:

$$\frac{1}{\Lambda_0^2} = \left(\frac{\pi}{L}\right)^2 + \left(\frac{2.405}{R}\right)^2, \quad (8)$$

where L and R are the chamber height and radius respectively. Λ_0 takes the value 4.9 cm. The first term on the right-hand side of equation (7) accounts for the time to diffuse to the chamber wall whilst the second corresponds to the time taken to react once the wall is reached. Diffusion coefficients are taken, with temperature dependences, from Winn [46] for molecules and from Morgan and Schiff [47] for atoms. We also assume that electronic excitation does not change the diffusion coefficient.

The crucial variable in equation (7) is the so called sticking coefficient or loss coefficient, γ , and the values used here are given table 3. We have previously reported values for γ in our aluminium chamber for both $O(^3P)$ [12] and $O_2(a^1\Delta_g)$ [30], obtained by monitoring the ringdown time after the plasma was extinguished. In both cases a value of ~ 0.003 was determined indicating that diffusion is relatively fast and reaction at the wall is rate determining. The Chantry formalism allows wall loss measurements under one set of conditions to be reasonably extrapolated to other operating conditions. The formalism

Table 2. Heavy species reactions and rate coefficients (T_{trans} in K).

#	Reaction	Rate coefficient/cm ³ s ⁻¹	Source
23	$\text{O}^- + \text{O}_2^+ \rightarrow \text{O}(\text{}^3\text{P}) + \text{O}_2(\text{}^3\Sigma_g^-)$	$3.2 \times 10^{-7} T_{\text{trans}}^{-0.44}$	[40]
24	$\text{O}^- + \text{O}_2^+ \rightarrow 3\text{O}(\text{}^3\text{P})$	$3.2 \times 10^{-7} T_{\text{trans}}^{-0.44}$	[40]
25	$\text{O}^- + \text{O}_2(\text{}^1\Delta_g) \rightarrow \text{O}_3 + \text{e}^-$	3.30×10^{-11}	[40]
26	$\text{O}^- + \text{O}_2(\text{}^1\Sigma_g^+) \rightarrow \text{O}_2(\text{}^3\Sigma_g^-) + \text{O}(\text{}^3\text{P}) + \text{e}^-$	6.9×10^{-10}	[40]
27	$\text{O}^- + \text{O}(\text{}^3\text{P}) \rightarrow \text{O}_2(\text{}^3\Sigma_g^-) + \text{e}^-$	1.6×10^{-10}	[40]
28	$\text{O}(\text{}^1\text{D}) + \text{O}_2(\text{}^3\Sigma_g^-) \rightarrow \text{O}(\text{}^3\text{P}) + \text{O}_2(\text{}^1\Delta_g)$	$1.6 \times 10^{-12} 2009 \exp(67/T_{\text{trans}})$	[48, 49]
29	$\text{O}(\text{}^1\text{D}) + \text{O}_2(\text{}^3\Sigma_g^-) \rightarrow \text{O}(\text{}^3\text{P}) + \text{O}_2(\text{}^1\Sigma_g^+)$	$2.56 \times 10^{-11} \exp(67/T_{\text{trans}})$	[48, 49]
30	$\text{O}(\text{}^1\text{D}) + \text{O}_2(\text{}^3\Sigma_g^-) \rightarrow \text{O}(\text{}^3\text{P}) + \text{O}_2(\text{}^3\Sigma_g^-)$	$4.8 \times 10^{-12} \exp(67/T_{\text{trans}})$	[48, 49]

Table 3. Wall reactions and loss coefficients.

#	Reaction	Γ	Source
31	$\text{O}_2(\text{}^1\Delta_g) + \text{wall} \rightarrow \text{O}_2(\text{}^3\Sigma_g^-)$	0.003	[30]
32	$\text{O}_2(\text{}^1\Sigma_g^+) + \text{wall} \rightarrow \text{O}_2(\text{}^3\Sigma_g^-)$	0.2	See text
33	$\text{O}(\text{}^3\text{P}) + \text{wall} \rightarrow 1/2 \text{O}_2(\text{}^3\Sigma_g^-)$	0.003	[12]
34	$\text{O}(\text{}^1\text{D}) + \text{wall} \rightarrow \text{O}(\text{}^3\text{P})$	1	See text

is however, an approximation, and strictly applies only when the plasma is well described by a single temperature. In our case, the emission and CRDS measurements demonstrate that the plasma temperature is inhomogeneous, and so we must proceed cautiously with the use of the Chantry equation.

For both $\text{O}(\text{}^3\text{P})$ [12] and $\text{O}_2(\text{}^1\Delta_g)$ [30] the second term in equation (7) dominates, and as this term is only weakly temperature dependent, $\nu \propto T^{1/2}$, the approximation works reasonably well. For $\text{O}_2(\text{}^1\Sigma_g^+)$ however, the first term in equation (7) is significant and has a much stronger temperature dependence (from kinetic theory [50] $D \propto T^{3/2}$). This means that at 100 mTorr, the temperature inhomogeneity significantly changes how $\text{O}_2(\text{}^1\Sigma_g^+)$ diffuses and this impacts the wall loss rate. Specifically, much of the $\text{O}_2(\text{}^1\Sigma_g^+)$ will exist in the hot centre of the chamber and will be at a temperature above the average and therefore diffuse out of this region more rapidly than equation (7) predicts. Indeed using our CRDS derived average temperature (429 K at 200 W) and diffusion coefficients from Winn, the Chantry equation predicts a minimum ($\gamma = 1$) wall loss lifetime of 7.5 ms at 100 mTorr. This value is longer than the observed lifetime of 6.7 ms and indicates the breakdown of the Chantry approximations.

This difficulty can be overcome by moving into a regime where the plasma is more spatially uniform and diffusion to chamber walls is faster (so that the first term in equation (7) becomes less significant). This can be achieved by operating at a lower pressure, and a temporal decay in $\text{O}_2(\text{}^1\Sigma_g^+)$ emission at 10 mTorr yields a lifetime of 2.4 ms and allows extraction of a more reasonable wall loss coefficient of $\gamma = 0.2$. Further measurements at 20 mTorr yield the same value, suggesting there is little variation of γ with pressure and hence that $\gamma = 0.2$ is likely to be a realistic value for wall loss of $\text{O}_2(\text{}^1\Sigma_g^+)$. In terms of other excited singlet species of relevance in the plasma, it is common to assume that the reactive

$\text{O}(\text{}^1\text{D})$ is lost at the walls with a coefficient of unity [11, 36] and we adopt that assumption here.

Using this reaction set, a series of kinetic balances are established whereby the rates of production and destruction of each species must be equal. Balances are constructed for $\text{O}_2(\text{}^1\Delta_g)$, $\text{O}_2(\text{}^1\Sigma_g^+)$, $\text{O}(\text{}^3\text{P})$, $\text{O}(\text{}^1\text{D})$ and O^- , also included are a pressure balance (i.e. the sum of partial pressures of the important species equals the total pressure) and a charge balance ($[\text{e}^-] + [\text{O}^-] = [\text{O}_2^+]$). This set of seven simultaneous equations are then solved (for a given T_{trans} , T_e and electron density, $[\text{e}^-]$) for the seven variables: $[\text{O}_2(\text{}^3\Sigma_g^-)]$, $[\text{O}_2(\text{}^1\Delta_g)]$, $[\text{O}_2(\text{}^1\Sigma_g^+)]$, $[\text{O}(\text{}^3\text{P})]$, $[\text{O}(\text{}^1\text{D})]$, $[\text{O}^-]$ and $[\text{O}_2^+]$. By varying T_e and $[\text{e}^-]$ the values that best reproduce experimental measurements of $[\text{O}_2(\text{}^1\Delta_g)]$ and $[\text{O}(\text{}^3\text{P})]$ can be found and likely densities of other species inferred. We note that the threshold energy for producing $\text{O}_2(\text{}^1\Delta_g)$ (via reaction 13) is 0.98 eV whilst the threshold for atom production (reaction 1) is ~ 5 eV. The densities of these species are therefore sensitive to different regions of the EEDF and the model must reflect this.

4.2. Choice of gas temperature for modelling

We wish to reproduce absolute line-of-sight averaged densities ($[\text{O}(\text{}^3\text{P})]$ and $[\text{O}_2(\text{}^1\Delta_g, \nu = 0)]$) and choose to use the line-of-sight averaged temperatures, T_{trans} , from the CRDS measurements of $\text{O}(\text{}^3\text{P})$ as inputs to our model (rather than choosing the elevated temperatures observed in emission). However, as noted earlier, the CRDS derived values for T_{trans} have significant uncertainties, and we therefore fit a spline to the emission derived temperatures which have smaller uncertainties (shown in blue in figure 2(b)) and scale this function to fit the CRDS data (shown in blue in figure 3(b)). This allows us to estimate a smoothly varying line-of-sight averaged temperature using the CRDS measurements but taking advantage of the better signal to noise ratio offered by the emission data.

5. Modelling results

5.1. Electron densities and temperatures

The modelled values for T_e and $[\text{e}^-]$ that were found to best reproduce the measured $[\text{O}(\text{}^3\text{P})]$ and $[\text{O}_2(\text{}^1\Delta_g, \nu = 0)]$ are shown in figure 5. Both quantities show a sharp rise during the E–H

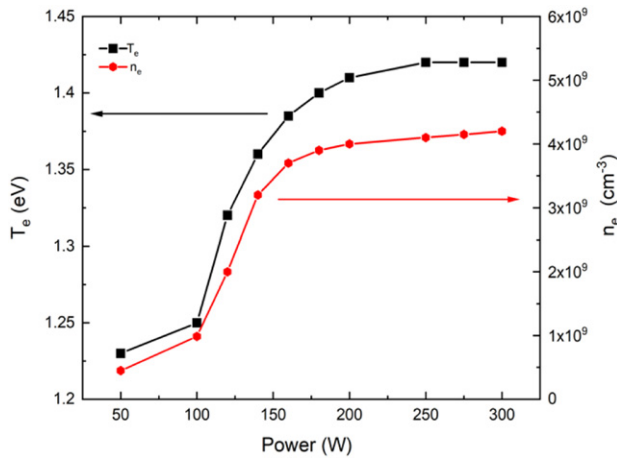


Figure 5. Electron densities and temperatures as predicted by the kinetic model as a function of plasma power.

switchover, with $[e^-]$ increasing by ca. an order of magnitude (up to $\sim 4.2 \times 10^9 \text{ cm}^{-3}$) over the power range. T_e undergoes a more modest increase (from ~ 1.23 to $\sim 1.42 \text{ eV}$). Within the H-mode, $[e^-]$ and T_e continue to increase only gradually.

5.2. Neutral species (general remarks)

Figure 6 shows the variation in densities predicted by the kinetic model for all the species (note the logarithmic ordinate scale). By far the most abundant species are the three lowest lying molecular states (X , a and b) and the ground state atoms, all of which are more than two orders of magnitude more abundant than the next most abundant species. A comparison of the predicted $[O(^3P)]$, $[O_2(a)]$ and $[O_2(b)]$ and their experimentally determined values are shown in figure 7. It should be noted that while the measured values for $[O(^3P)]$ and $[O_2(a)]$ are absolute (from CRDS data), those for $O_2(b^1\Sigma_g^+)$ are not; they are instead taken from the inset to figure 2(a) and scaled, to show that the model predicts a reasonable trend in $[O_2(b)]$. The important processes producing and destroying each species are now considered in turn.

5.2.1. $O_2(X^3\Sigma_g^-)$. The ground state of O_2 is the only species whose density decreases monotonically with increasing power, see figure 6. Being the precursor to all other species formed within the plasma, $[O_2(X)]$ necessarily decreases when the densities of other species increases. This is most notable during the switchover where $[O_2(X)]$ drops most rapidly as the rates of electron impact driven processes markedly increase. Within the H-mode, where excited state densities change relatively little compared to the switchover region, the depletion of $[O_2(X)]$ is instead dominated by gas heating and resulting gas dilution.

5.2.2. $O_2(a^1\Delta_g)$. In the E-mode $O_2(a^1\Delta_g)$ is predominantly produced by electron impact excitation of $O_2(X^3\Sigma_g^-)$ (reaction 13), and lost at the chamber walls (reaction 31). As power increases (and $[e^-]$ rises) within the E-mode, produc-

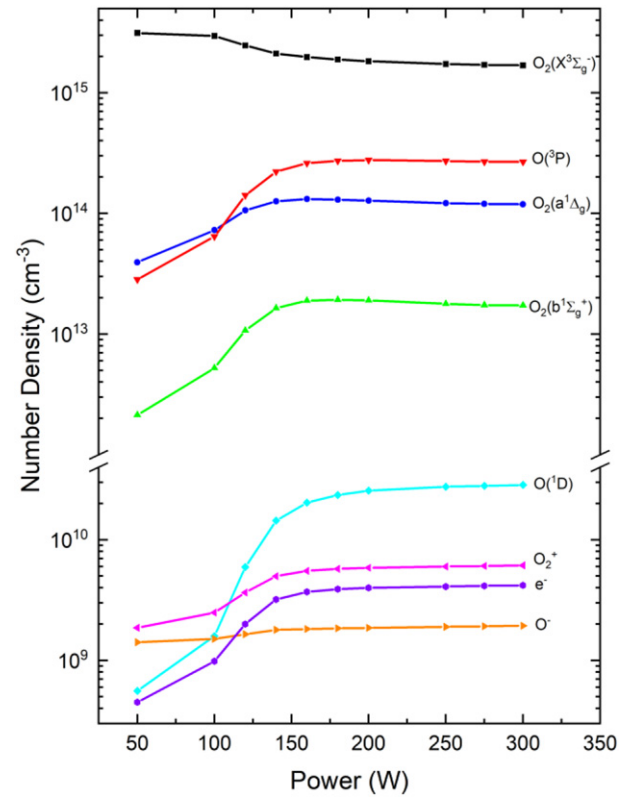


Figure 6. Number densities of all modelled species as a function of plasma power.

tion increases rapidly and wall loss remains approximately constant hence the rapid increase in $[O_2(a)]$. Within the H-mode however electron impact de-excitation of $O_2(b^1\Sigma_g^+)$ (reaction 18), also becomes a significant production process ($\sim 20\%$ of the total at 300 W) while electron impact excitation to $O_2(b^1\Sigma_g^+)$ (reaction 17), and de-excitation to $O_2(X^3\Sigma_g^-)$ (reaction 14) become significant loss processes ($\sim 36\%$ and $\sim 18\%$ of the total loss respectively at 300 W).

Electron impact therefore becomes important for both production and destruction, thus $[O_2(a)]$ appears less dependent on $[e^-]$ in the H-mode than in E-mode. The reduction in $[O_2(a)]$ as power increases in the H-mode is therefore predominantly a result of gas heating decreasing $[O_2(X)]$ (the main precursor to $O_2(a^1\Delta_g)$). We note that, as power increases, the measured density drops below that which we predict by the model. This can be accounted for by noting that the measured values are only of $v = 0$ while the model does not discriminate vibrational levels; as power increases, so does T_{vib} and the discrepancy between the values also increases. Using our T_{vib} value of 905 K measured by emission spectroscopy at 300 W, we estimate the total density of $O_2(a^1\Delta_g)$ across all vibrational states to be $(1.19 \pm 0.15) \times 10^{14} \text{ cm}^{-3}$ in good agreement with the modelled value and shown by the filled blue circle in figure 7. This calculation suggests that, even at our highest power, more than 90% of the a state exists in the vibrational ground state. Our decision not to include vibrational excitation in the volume averaged model therefore seems reasonable.

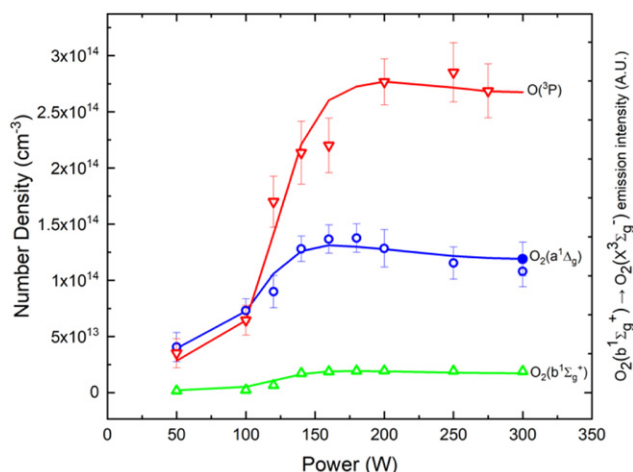


Figure 7. Number densities of $O(^3P)$ (red), $O_2(a^1\Delta_g)$ (blue) and $O_2(b^1\Sigma_g^+)$ (green) as a function of plasma power as predicted by the model (solid lines) and compared to values derived from experiments (unfilled points). For $O(^3P)$ and $O_2(a^1\Delta_g)$ experimental values are absolute measurements made by CRDS, for $O_2(b^1\Sigma_g^+)$ the values are relative densities derived from emission spectra. The filled blue circle represents the density corrected for vibrational excitation, see text.

5.2.3. $O_2(b^1\Sigma_g^+)$. For $O_2(b^1\Sigma_g^+)$ in the E-mode several production processes are important: electron impact excitation both from $O_2(X)$ and $O_2(a^1\Delta_g)$ (reactions 15 and 17 respectively) and the quenching of $O(^1D)$ by $O_2(X^3\Sigma_g^-)$ (reaction 29) which contribute in a $\sim 35:15:50$ ratio respectively at 50 W. As was the case for $O_2(a^1\Delta_g)$, loss is once again dominated by quenching at the chamber wall and so the same arguments hold for explaining the rapidly increasing $[O_2(b)]$ in the switchover region (noting that both $[e^-]$ and $[O(^1D)]$ increase rapidly during the switchover, so all production processes increase markedly in rate).

In the H-mode the same three production processes remain most important but now with respective relative rates $\sim 15:25:60$ at 300 W. Wall loss is still the predominant loss process, but electron impact de-excitation to $O_2(a^1\Delta_g)$ (reaction 18) now makes a contribution of $\sim 15\%$. This means that the most important production and loss processes in the H-mode are not direct electron impact based reactions and $[O_2(b)]$ in the H-mode is not greatly influenced by the small changes in $[e^-]$. Once again temperature effects, i.e. gas dilution, dominate and the density decreases as power increases due to a depletion of the $O_2(X^3\Sigma_g^-)$ precursor.

5.2.4. $O(^3P)$. The predominant loss process for $O(^3P)$ is reaction at chamber walls (reaction 33) under all conditions. At the highest powers the rate of electron impact excitation to $O(^1D)$ (reaction 19) is competitive with wall loss, but as all $O(^1D)$ is subsequently quenched back to $O(^3P)$ this is not a net loss process for $O(^3P)$. In the E-mode, production of $O(^3P)$ is predominantly by electron impact dissociation (EID) of $O_2(X^3\Sigma_g^-)$ (reactions 1 and 4) and by dissociative electron attachment (DEA) to $O_2(X^3\Sigma_g^-)$ (reaction 7). All three play important roles with relative ratios of 63:32:5. Production

processes involving electronically excited molecules account for $<3\%$ of the total production at 50 W.

In the H-mode EID with $O_2(a^1\Delta_g)$ (reaction 2) and quenching of $O(^1D)$ by $O_2(X^3\Sigma_g^-)$ (reactions 28, 29 and 30) also become important production processes for $O(^3P)$. Note, although some of the $O(^1D)$ quenching simply offsets reaction 19, some of the $O(^1D)$ originates instead from reaction 4 and the net effect of the quenching reactions (28–30) with reaction 4 is the production of $O(^3P)$. In the H-mode therefore, the $[O(^3P)]$ becomes less dependent on $[e^-]$ and is once again influenced most strongly by gas heating.

5.2.5. $O(^1D)$. Modelled $[O(^1D)]$ are shown in figure 6. Across the power range $O(^1D)$ is predominantly lost through quenching by $O_2(X^3\Sigma_g^-)$ (reactions 28–30) while its production is dominated by EID of $O_2(X^3\Sigma_g^-)$ (reaction 4) and electron impact excitation of $O(^3P)$ (reaction 19). In the E-mode these account for 88% and 12% of production, respectively. In the H-mode their importance is swapped, accounting for 44% and 54%, respectively (the remaining 2% is by EID of $O_2(a^1\Delta_g)$ and $O_2(b^1\Sigma_g^+)$ (reactions 5 and 6)). $O(^1D)$ is therefore produced exclusively by electron impact and destroyed without the need for electrons across the entire operating range. $[O(^1D)]$ therefore shows no maximum at high powers but instead continues to rise with $[e^-]$ across the power range. Gas heating has little influence on $[O(^1D)]$ because $O_2(X^3\Sigma_g^-)$ acts not only as a precursor, but also as a quencher of $O(^1D)$.

5.3. Ions and electronegativity

The predicted behaviour of charged species with plasma power is shown in figure 8. Also shown is the change in electronegativity, EN , the ratio of negative ion density to electron density, and one experimental value for the $[O^-]$, measured using the O^- photodetachment continuum at 630 nm [12] (unfilled pentagon).

5.3.1. O^- and electronegativity. At low power the major production route of O^- is DEA with $O_2(X^3\Sigma_g^-)$ (reaction 7) whilst it is predominantly lost by electron detachment with metastable molecules and $O(^3P)$ atoms (reactions 25–27).

Within the E-mode the densities of the quenching species are low, meaning that O^- is relatively long lived (compared to electrons) and is effectively a reservoir of negative charge. As power increases the densities of both electrons (responsible for producing O^-) and the excited species responsible for quenching O^- increase. And so while $[e^-]$ increases by an order of magnitude across the power range, $[O^-]$ undergoes a much more modest increase of $\sim 40\%$. The $[O^-]$ predicted by the model agrees well with our previous measurement of the species in this chamber under the same conditions.

This behaviour is reflected in the predicted EN . In the E-mode EN is high because O^- has a low quenching rate. As power increases the increasing $[e^-]$ is not mirrored in $[O^-]$ (despite faster O^- production) because the rate of quenching also increases, and leads to a lower EN that shows much

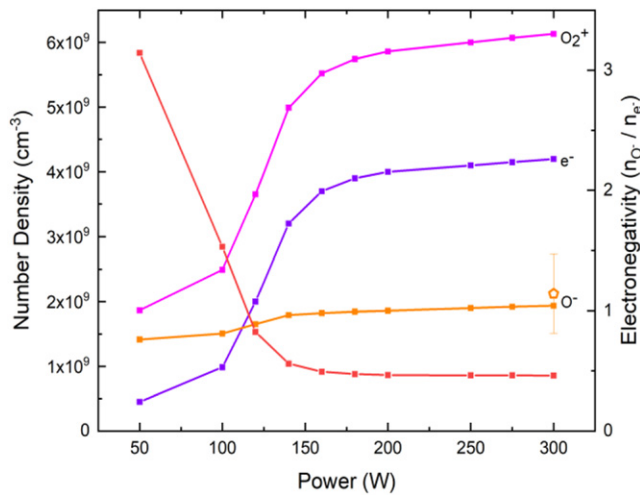


Figure 8. Densities of charged plasma species as a function of plasma power as predicted by the model, also shown in red is the electronegativity (ratio of negative ion to electron density). The pentagonal point is an experimental O^- density taken from CRDS measurement of the O^- photodetachment continuum at 630 nm [12].

less variation with plasma power in the H-mode than it does in the E-mode. Across all powers the EN is significantly above zero indicating that ions are always a significant reservoir of negative charge, as would be expected for an oxygen system. The fall in EN we observe across the E/H-mode transition from ~ 3 to ~ 0.5 is consistent with previous work [51].

5.3.2. O_2^+ . The model includes no kinetic balance for O_2^+ because its wall loss rate in our chamber is unknown (and is likely to be significant [36]); instead its density is defined by quasi-neutrality. This makes detailed discussion of its kinetics difficult but the expectation is that O_2^+ is predominantly produced by electron impact ionisation of $O_2(X^3\Sigma_g^-)$ (reactions 10–12) and predominantly lost at the walls. This would correspond to a loss rate that is invariant with changing $[e^-]$ and a production rate directly proportional to $[e^-]$. This is in good agreement with the model's prediction that $[O_2^+]$ follows $[e^-]$ very closely.

5.4. Effects of gas temperature

The modelled results are calculated using the temperatures that are found as described in the previous sections. It should be noted however, that the reaction set itself is actually only weakly dependent on gas temperature. Reactions in table 2 all have only weak temperature dependences whilst the wall loss rates for $O(^3P)$ and $O_2(a^1\Delta_g)$ vary by less than 20% for a temperature increase from 460 K to 630 K (the temperatures from CRDS and emission experiments, respectively). Even the wall loss rates for $O_2(b^1\Sigma_g^+)$ and $O(^1D)$ which have the strongest temperature dependence only increase by $\sim 60\%$ as the temperature increases from 460 K to 630 K, and seeing as there are no absolute measurements of their densities with which to compare, this makes little difference to the conclusions we can draw from our model.

In fact, by far the most important influence of using the elevated emission temperatures for modelling would be the resulting drop in the density of all species, reflecting the ideal gas law. It is found, across the modelled power range, that when the higher temperatures are used good agreement between experimental and modelled number densities can still be achieved simply by increasing $[e^-]$. In the E-mode, where temperatures differ less between the two experiments, $[e^-]$ must be increased by $\sim 30\%$ to achieve good agreement, whilst in the H-mode an increase of $\sim 60\%$ in $[e^-]$ is required to achieve good agreement. In the context of the simplifying assumptions inherent in the volume averaged model these changes in $[e^-]$ represent a minor adjustment. Thus, the quantitative conclusions we draw from our model in the cases of $O(^3P)$ and $O_2(a^1\Delta_g)$ are almost independent of the gas temperatures we use. Likewise, the more qualitative discussion as to the most important processes controlling densities of other species are also valid regardless of our choice of temperature.

6. Discussion

The majority of previous work utilising emission from O_2 plasmas as a diagnostic tool has focused on strong atomic emission (e.g. at 777 and 844 nm). Such emission has been used in particular for actinometric [37, 52] and TALIF [13] based determination of atom densities (via non-trivial calibration processes). Molecular emission bands, can yield quantitative information, namely temperatures T_{rot} and T_{vib} , with the former expected to be in equilibrium with the translational temperature T_{trans} , but again absolute concentrations cannot be easily determined.

Plasma emission comes predominantly from the regions of the plasma where electron impact excitation is largest [3] (i.e. in the centre of the chamber); these regions are also expected to have the highest gas temperature, such that temperatures derived from emission data are more representative of the temperature at the centre of the chamber. It is therefore significant that our emission based T_{rot} values (629 ± 10 K at 300 W) agree well with that from Kiehlbauch and Graves [3] for the gas phase neutral temperature (~ 600 K for 300 W) whilst our line-of-sight averaged temperature from CRDS spectra (440 ± 25 K at 300 W) are intermediate between the gas phase temperature of Kiehlbauch and Graves and the temperature they calculate close to the chamber wall (~ 375 K at 300 W), observations attributable to the thermal inhomogeneity of the plasma. Our emission temperatures are also in good agreement with other previous work utilising emission spectroscopy [2].

That the plasma exhibits thermal inhomogeneity is also manifest in the inapplicability of the Chantry formulism to our observations at 100 mTorr, resulting in the need to reduce the plasma pressure in order to obtain physically reasonable wall loss coefficients for $O_2(b^1\Sigma_g^+)$. It is of interest to compare our wall loss coefficient, $\gamma = 0.2$, with previous literature values. Wayne [53] reported that γ lies between 0.002 and 0.04 for a variety of surfaces (none of them aluminium) whilst the more

recent work of Perram *et al* [54] found a value of 0.007 for aluminium (although in that work it was assumed that $O_2(a^1\Delta_g)$ was formed by loss of $O_2(b^1\Sigma_g^+)$ at the walls). Meichsner and Wegner [11] found that a value of $\gamma = 0.007$ for $O_2(b^1\Sigma_g^+)$ wall loss was self consistent, within a volume averaged model, at reproducing experimentally measured $[O_2(a)]$ determined in a stainless steel chamber. However, they also found that $[O_2(b)]$ was expected to exceed the $[O_2(a)]$ in the H-mode, something which simply does not occur in our plasma - if it did we would see evidence of stimulated emission on the Noxon band rather than the absorption we actually observe [30]. Our previous measurements of $O_2(a^1\Delta_g)$ corroborate that 0.007 is far too low a value of γ for $O_2(b^1\Sigma_g^+)$ in our chamber. Several other modellers [11, 36, 55] have used the significantly higher value of 0.1. This is in much better agreement with our observations and with the recent work of Booth *et al* [43] which found a value of 0.135. The value of 0.1 originates from an assertion that wall loss of $O_2(b^1\Sigma_g^+)$ ought to be between 10 and 100 times faster than the same process for $O_2(a^1\Delta_g)$ [56, 57]. Our measurements of sticking coefficients for both species are in agreement with this assertion, with the ratio between the two coefficients for our chamber found to be ~ 66 .

Vibrational temperatures, T_{vib} , in oxygen ICPs are expected to be higher than T_{rot} and T_{trans} due to the more efficient transfer of energy from electrons into vibrational modes. They are however expected to be lower than the T_{vib} values observed in N_2 plasmas (where resonant vibrational excitation via the $N_2^-(X)$ state makes electron to vibration energy transfer extremely efficient). Our measured value of 905 ± 40 K sits in this regime, between ~ 460 K for an average T_{trans} , and ~ 3000 K measured for N_2 plasma under similar conditions in the same chamber [58]. This value also compares favourably with effective T_{vib} values that can be estimated (for low v levels) from the vibrational distribution function of Annusova *et al* [59]. At 80 mTorr and 500 W these researchers predict a ratio of $v = 0$ to $v = 1$ populations to be approximately 10, corresponding to a $T_{vib} \sim 1000$ K. We also note that Annusova *et al* report significantly non-thermal vibrational population distributions which indicates that our vibrational temperature is likely to underestimate the populations of higher lying vibrational levels. However, given that these high lying states are predominantly lost by V-T energy transfer with $O(^3P)$ and we have observed significantly higher atom densities than those modelled by Annusova *et al*, it is likely that these vibrationally excited molecules account for a very small proportion of the total molecular density and thus ignoring this higher vibrational excitation (and its non-thermal nature) makes little difference to inferred total densities of $O_2(a^1\Delta_g)$.

The observed increase in $[O(^3P)]$ by an order of magnitude in switching from the E-to the H-mode, is in good agreement with a number of previous workers. However, the absolute densities are significantly higher than those found by others [11, 59] and is directly attributable to the significantly smaller wall loss coefficient for our chamber.

Our new CRDS results on $O(^3P)$ show two differences compared to our previous report at 300 W using the same technique

in the same chamber [12], most notably in the lower number density but higher temperature (460 K here compared to 340 K previously) of the atoms. Having reviewed data veracity and acquisition protocols from both measurement ‘campaigns’ and found no operational inconsistencies or irregularities likely to have caused this discrepancy, we are of the opinion that both datasets are an accurate reflection of $[O(^3P)]$ and line-of-sight average temperatures characteristic of the plasma at the time the data were taken. The only potentially significant change in the plasma chamber between our previous measurements and those presented here could have been caused by the cleaning of the chamber’s internal surfaces. Thus, a potential explanation of the discrepancies between previous measurements and those presented here is that the cleaning significantly changed the thermal accommodation properties of the surfaces, for example by removing or reducing the thickness of the oxide layer that tends to exist on such walls. This could have a significant impact on the plasma temperature and atom temperature and density, as discussed by Gibson *et al* [60]. The observed temperature increase results in a $\sim 30\%$ increase in the rate of wall loss of $O(^3P)$, by increasing both the diffusion constant and mean thermal velocity (and assuming an unchanged wall loss coefficient of 0.003), and a $\sim 35\%$ decrease in the production rate of $O(^3P)$ because the heating also depletes $O_2(X^3\Sigma_g^-)$ through gas dilution. Combined, these changes reduce $[O(^3P)]$ by $\sim 50\%$, in very good agreement with the reduction in density we observe. Thus the reduced number density can be rationalised entirely by the temperature change and is not due to a change in the wall loss coefficient.

We note that our previous CRDS work probing $O_2(a^1\Delta_g)$ also shows a gas temperature lower than that measured here ($T_{rot} = 350 \pm 40$ K) and is attributable to the greater penetration of $O_2(a^1\Delta_g)$ into the cool steel baffle arms of the chamber used in the present experiments. $O(^3P)$ has a wall loss coefficient on steel of ~ 0.15 [61] and thus penetrates ~ 0.5 cm into the baffle arms [12]. Meanwhile $O_2(a^1\Delta_g)$ has a much smaller wall loss coefficient on steel of ~ 0.007 [30, 62] and is thus able to penetrate much further into the arms (~ 5 cm) [30]. This means that a much greater proportion of the $O_2(a^1\Delta_g)$ absorption results from gas that has had opportunity to thermally equilibrate with the chamber walls, hence the lower line-of-sight average temperature. It is of significance that the complementary data for the two species provides insight into their spatial distributions even though the CRDS technique itself is not spatially resolved.

To reiterate, the validity of quantitative conclusions arising from any kinetic plasma model is invariably limited by the certainty with which the plasma chemistry is understood. In the case of the model used here the fact that electron temperatures and densities are adjustable model input parameters means that, to a degree, deficiency in the chemistry set can be compensated for by changes in electron temperature and density. Nevertheless, the validity of the model can be assessed by comparing the optimal electron temperatures and densities it requires to best reproduce the observations against other measurements.

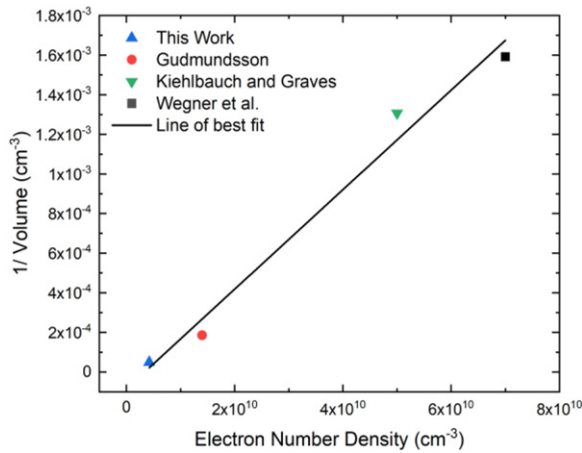


Figure 9. Plot demonstrating the linear relationship between modelled electron densities and the inverse of the plasma volume; all points are for a 100 mTorr 300 W plasma.

Many researchers have modelled or measured values for T_e and $[e^-]$ in O_2 plasmas under conditions similar or identical to those investigated here. Much of the literature work was carried out using (or modelling) chambers considerably smaller than ours, i.e. with electrode separations <10 cm and perhaps unsurprisingly much of this work results in $[e^-]$ values somewhat higher than we predict in our chamber for the same power. The highest literature values are $\sim 10^{11} \text{ cm}^{-3}$ in chambers with small volumes operating at low pressures <30 mTorr [1, 55]. Slightly lower $[e^-]$ values ($\sim \text{a few} \times 10^{10} \text{ cm}^{-3}$) are found in chambers that are either smaller than ours [2, 3, 11] or operate at lower pressures [4, 5], whilst the lowest literature values ($\sim 5 \times 10^9$ – $\sim 10^{10} \text{ cm}^{-3}$) most comparable with our own value of $4.2 \times 10^9 \text{ cm}^{-3}$ at 300 W are found in a chamber much bigger than ours [6] and in plasmas that differ from ours only in their volume [7] or power [8, 36]. This comparison is exemplified by figure 9 which demonstrates how modelled or measured $[e^-]$ changes with plasma volume (calculated simply as the chamber volume except in one case [2] where the chamber is significantly larger than the discharge region volume and as such the volume between the two electrodes was instead used). Most notably these literature data are chosen because they either present directly [3, 7] or allow straightforward estimation of [2] $[e^-]$ at 300 W power and 100 mTorr pressure. The results show quite convincingly that the $[e^-]$ in an O_2 plasma scales inversely with plasma volume if power and pressure are kept constant and that, given this relationship, our modelled $[e^-]$ fall in line with those found in other chambers.

The electron temperatures derived from the model lie between 1.2 and 1.42 eV. These values are somewhat lower than those measured in similar pure oxygen discharges with values typically between 2 and 4 eV [1, 2], albeit with higher power densities. Some previous work however, falls in line with the model values found here, in particular the work of Toneli *et al* [8] which models an electron temperature (assuming a Maxwellian EEDF) of less than 2 eV for a 100 mTorr and 500 W plasma and the work of Seo and Chung [6] who measure an electron temperature of 1.4 eV in a 40 mTorr

400 W plasma (and might expect an even lower electron temperature at higher pressures). The electron temperatures found here are thus well within the bounds of previous work and, most compellingly of all, they are in rather good agreement with measurements made using a planar electrical probe in the same chamber which found electron temperatures of 1.6 eV at 100 mTorr and 400 W and also found electron densities of a few 10^9 cm^{-3} , also in good agreement with the model results [63].

Finally, we note that throughout our modelling, for the sake of simplicity, we assume a Maxwellian distribution of electron energies and this could certainly influence the electron temperature that our model returns. In particular a Maxwellian distribution typically overestimates the relative density of higher energy electrons and to compensate this it is possible that the model underestimates the effective electron temperature [8]. The assumption of a Maxwellian EEDF has however been shown to be a good approximation for the plasma H-mode [2] with just a small depletion of electrons at high energies (>15 eV [1]) whereas in the E-mode the Maxwellian approximation is less realistic (bi-Maxwellian and Druyvesteyn EEDF's being more realistic [1, 2]) and so our modelling is likely to be less reliable, although still qualitatively informative, in this regime.

7. Conclusions

We have utilised CRDS to study the absolute densities of oxygen atoms produced in an O_2 plasma operating at 100 mTorr as the power is varied between 50 and 300 W. This range encompasses the E–H mode transition and the line-of-sight averaged $[O(^3P)]$ increases by an order magnitude from ca. $3 \times 10^{13} \text{ cm}^{-3}$ at 50 W to ca. $3 \times 10^{14} \text{ cm}^{-3}$ at 250 W; this general increase in number density is a non-linear function of power with a marked increase occurring around 120 W. Optical emission studies show that the global emission from the plasma also increases markedly at this power.

Wavelength resolved emission spectra of the A band allows determination of the rotational temperature, T_{rot} , of $O_2(b^1\Sigma_g^+)$ and this also increases markedly at the E–H transition. Interestingly, T_{rot} for the b state inferred from the emission studies (ca. 630 K at 300 W) are higher than the translational temperatures, T_{trans} , of the O atoms measured by CRDS (ca. 450 K at 300 W) and reflects both the differing volumes of the plasma that each technique samples and its inherent spatial inhomogeneity. Importantly, the dominant chemistry within the plasma is only weakly temperature dependent and any differences in temperature do not significantly affect the conclusions derived from kinetic modelling.

These new CRDS data on $O(^3P)$ have been combined with previously published CRDS data on the variation in density of $O_2(a^1\Delta_g, v=0)$ as a function of power to inform a volume averaged kinetic model based on a restricted number of important reactions. This modelling has allowed the electron number density across the operating conditions to be inferred. At 300 W, $[e^-]$ is $4 \times 10^9 \text{ cm}^{-3}$ and consistent with the (large) volume of our plasma chamber.

The agreement between the model results and the prior electrical probe measurements combined with the fact that the EEDF is expected to be close to Maxwellian in the H-mode provide confidence that the kinetic modelling describes the observed chemistry in a meaningful way despite the model's intrinsic limitations (e.g. being volume averaged).

The model also returns predicted densities for ionic species and in the case of O^- is in excellent agreement with previous CRDS photodetachment measurements. Finally, the work highlights the importance of surface chemistry in determining $[O(^3P)]$ in O_2 plasmas; simply cleaning our aluminium chamber led to a decrease in atomic density by 50% and was quantitatively accounted for by a concomitant increase in gas temperature. Similarly, we note that the wall loss coefficient for $O_2(b^1\Sigma_g^+)$ must be relatively high, here taking the value of 0.2.

Acknowledgments

The authors would like to acknowledge the UK Engineering and Physical Sciences Research Council (EPSRC) for support provided within the standard research scheme (Grant No. EP/P026621/1) and Lam Research Corporation (US) for a gift award. SDAR would like to thank the Clarendon fund for the award of a graduate scholarship.

Data availability statement

The data that support the findings of this study are available upon reasonable request from the authors.

ORCID iDs

Samuel D A Rogers  <https://orcid.org/0000-0002-5276-0920>

Amelia Bond  <https://orcid.org/0000-0002-9539-6698>

Benjamin J Rhodes  <https://orcid.org/0000-0002-6133-6531>

Robert Peverall  <https://orcid.org/0000-0003-2326-2495>

Gus Hancock  <https://orcid.org/0000-0003-1166-4104>

Grant A D Ritchie  <https://orcid.org/0000-0003-1663-7770>

References

- [1] Corr C S, Gomez S and Graham W G 2012 *Plasma Sources Sci. Technol.* **21** 055024
- [2] Wegner T, Küllig C and Meichsner J 2017 *Plasma Sources Sci. Technol.* **26** 025006
- [3] Kiehlbauch M W and Graves D B 2003 *J. Vac. Sci. Technol. A* **21** 660
- [4] Gudmundsson J T, Kimura T and Lieberman M A 1999 *Plasma Sources Sci. Technol.* **8** 22
- [5] Gudmundsson J T, Marakhtanov A M, Patel K K, Gopinath V P and Lieberman M A 2000 *J. Phys. D: Appl. Phys.* **33** 1323
- [6] Seo D C and Chung T H 2001 *J. Phys. D: Appl. Phys.* **34** 2854
- [7] Gudmundsson J T 2004 *J. Phys. D: Appl. Phys.* **37** 2073
- [8] Toneli D A, Pessoa R S, Roberto M and Gudmundsson J T 2015 *J. Phys. D: Appl. Phys.* **48** 495203
- [9] Mitsui Y and Makabe T 2021 *Plasma Sources Sci. Technol.* **30** 023001
- [10] Booth J P et al 2020 *Plasma Sources Sci. Technol.* **29** 115009
- [11] Meichsner J and Wegner T 2018 *Eur. Phys. J. D* **72** 85
- [12] Peverall R, Rogers S D A and Ritchie G A D 2020 *Plasma Sources Sci. Technol.* **29** 045004
- [13] Hancock G and Toogood M J 1992 *Appl. Phys. Lett.* **60** 35
- [14] Gomez S, Steen P G and Graham W G 2002 *Appl. Phys. Lett.* **81** 19
- [15] Jasik J, Macko P, Martisovits V, Lukac P and Veis P 2004 *Czech. J. Phys.* **54** 661
- [16] Booth J P, Joubert O, Pelletier J and Sadeghi N 1991 *J. Appl. Phys.* **69** 618
- [17] Peverall R and Ritchie G A D 2019 *Plasma Sources Sci. Technol.* **28** 073002
- [18] Niemi K, Schulz-von der Gathen V and Döbele H F 2001 *J. Phys. D: Appl. Phys.* **34** 2330
- [19] Niemi K, O'Connell D, de Oliveira N, Joyeux D, Nahon L, Booth J P and Gans T 2013 *Appl. Phys. Lett.* **103** 034102
- [20] Yang X, Sasaki K and Nagatsu M 2015 *Plasma Sources Sci. Technol.* **24** 055019
- [21] Harris S J and Weiner A M 1981 *Opt. Lett.* **6** 142
- [22] Teslja A and Dagdigian P J 2004 *Chem. Phys. Lett.* **400** 374
- [23] Gupta M, Owano T, Baer D and O'Keefe A 2006 *Appl. Phys. Lett.* **89** 241503
- [24] Hancock G, Peverall R, Ritchie G A D and Thornton L J 2007 *J. Phys. D: Appl. Phys.* **40** 4515
- [25] Pazyuk V S, Podmar'kov Y P, Raspopov N A and Frolov M P 2001 *Quantum Electron.* **31** 363
- [26] Gupta M, Owano T, Baer D S, O'Keefe A and Williams S 2004 *Chem. Phys. Lett.* **400** 42
- [27] Williams S, Gupta M, Owano T, Baer D S, O'Keefe A, Yarkony D R and Matsika S 2004 *Opt. Lett.* **29** 1066
- [28] Williams S, Popovic S and Gupta M 2009 *Plasma Sources Sci. Technol.* **18** 035014
- [29] Földes T, Čermák P, Macko M, Veis P and Macko P 2009 *Chem. Phys. Lett.* **467** 233
- [30] Rogers S D A, Bond A, Peverall R, Hancock G, Western C M and Ritchie G A D 2021 *Plasma Sources Sci. Technol.* **30** 09LT02
- [31] Romanini D, Kachanov A A and Stoeckel F 1997 *Chem. Phys. Lett.* **270** 538
- [32] Western C M 2017 *J. Quant. Spectrosc. Radiat. Transfer* **186** 221
- [33] Yu S, Drouin B J and Miller C E 2014 *J. Chem. Phys.* **141** 174302
- [34] Drouin B J et al 2017 *J. Quant. Spectrosc. Radiat. Transfer* **186** 118
- [35] Baluja K L and Zeippen C J 1988 *J. Phys. B: At. Mol. Opt. Phys.* **21** 1455
- [36] Toneli D A, Pessoa R S, Roberto M and Gudmundsson J T 2015 *J. Phys. D: Appl. Phys.* **48** 325202
- [37] Fuller N C M, Malyshev M V, Donnelly V M and Herman I P 2000 *Plasma Sources Sci. Technol.* **9** 116
- [38] Phelps A V 1985 Tabulations of collision cross sections and calculated transport and reaction coefficients for electron collisions with O_2 *Technical Report 28, JILA Information Center Report* (Boulder, Colorado: University of Colorado)
- [39] Laporta V, Celiberto R and Tennyson J 2015 *Phys. Rev. A* **91** 012701
- [40] Gudmundsson J T 2004 A critical review of the reaction set for a low pressure oxygen processing discharge *Technical Note* (Science Institute, University of Iceland)
- [41] Tashiro M, Morokuma K and Tennyson J 2006 *Phys. Rev. A* **73** 052707
- [42] Peverall R et al 2001 *J. Chem. Phys.* **114** 6679

- [43] Booth J P *et al* 2022 *Plasma Sources Sci. Technol.* **31** 065012
- [44] Volynets A V, Lopaev D V, Rakhimova T V, Proshina O V, Chukalovsky A A and Booth J P 2020 *Plasma Sources Sci. Technol.* **29** 115020
- [45] Chantry P J 1987 *J. Appl. Phys.* **62** 1141
- [46] Winn E B 1950 *Phys. Rev.* **80** 1024
- [47] Morgan J E and Schiff H I 1964 *Can. J. Chem.* **42** 2300
- [48] Atkinson R, Baulch D L, Cox R A, Hampson R F Jr, Kerr J A, Rossi M J and Troe J 1997 *J. Phys. Chem. Ref. Data* **26** 521
- [49] Liu D X, Rong M Z, Wang X H, Iza F, Kong M G and Bruggeman P 2010 *Plasma Processes Polym.* **7** 846
- [50] Hirschfelder J O, Curtiss C F and Bird R B 1954 *Molecular Theory of Gases and Liquids* (New York: Wiley)
- [51] Wegner T, Küllig C and Meichsner J 2017 *Plasma Sources Sci. Technol.* **26** 025007
- [52] Lopaev D V, Volynets A V, Zyryanov S M, Zotovich A I and Rakhimov A T 2017 *J. Phys. D: Appl. Phys.* **50** 075202
- [53] Wayne R P 1969 *Advances in Photochemistry* vol 7 ed N Pitts (New York: Wiley) pp 311–71
- [54] Perram G P, Determan D A, Dorian J A, Lowe B F and Thompson T L 1992 *Chem. Phys.* **162** 427
- [55] Thorsteinsson E G and Gudmundsson J T 2010 *Plasma Sources Sci. Technol.* **19** 055008
- [56] Burrow P D 1973 *J. Chem. Phys.* **59** 4922
- [57] Vidaud P H, Wayne R P and Yaron M 1976 *Chem. Phys. Lett.* **38** 306
- [58] Hancock G, Peverall R, Ritchie G A D and Thornton L J 2006 *J. Phys. D: Appl. Phys.* **39** 1846
- [59] Annušová A, Marinov D, Booth J P, Sirse N, Lino da Silva M, Lopez B and Guerra V 2018 *Plasma Sources Sci. Technol.* **27** 045006
- [60] Gibson A R, Foucher M, Marinov D, Chabert P, Gans T, Kushner M J and Booth J P 2017 *Plasma Phys. Control. Fusion* **59** 024004
- [61] Gudmundsson J T and Thorsteinsson E G 2007 *Plasma Sources Sci. Technol.* **16** 399
- [62] Sharpless R L and Slanger T G 1989 *J. Chem. Phys.* **91** 7947
- [63] Bakowski B 2003 *Laser studies of species in plasma PhD Thesis* University of Oxford